



High-purity orbital angular momentum states from a visible metasurface laser

Hend Sroor¹, Yao-Wei Huang^{2,3}, Bereneice Sephton¹, Darryl Naidoo^{1,4}, Adam Vallés^{5,8}, Vincent Ginis^{2,5}, Cheng-Wei Qiu^{6,7}, Antonio Ambrosio^{6,7}, Federico Capasso^{6,7} and Andrew Forbes¹✉

Orbital angular momentum (OAM) from lasers holds promise for compact, at-source solutions for applications ranging from imaging to communications. However, conjugate symmetry between circular spin and opposite helicity OAM states ($\pm\ell$) from conventional spin-orbit approaches has meant that complete control of light's angular momentum from lasers has remained elusive. Here, we report a metasurface-enhanced laser that overcomes this limitation. We demonstrate new high-purity OAM states with quantum numbers reaching $\ell=100$ and non-symmetric vector vortex beams that lase simultaneously on independent OAM states as much as $\Delta\ell=90$ apart, an extreme violation of previous symmetric spin-orbit lasing devices. Our laser conveniently outputs in the visible, producing new OAM states of light as well as all previously reported OAM modes from lasers, offering a compact and power-scalable source that harnesses intracavity structured matter for the creation of arbitrary chiral states of structured light.

In recent years it has become possible to tailor light in what is commonly referred to as structured light¹, supporting applications including high-bandwidth optical communication^{2–5}, access to high-dimensional quantum states^{6,7}, enhanced resolution in imaging⁸ and microscopy⁹ and control of matter by optical trapping and tweezing^{10,11}. Foremost among the family of structured light fields are those related to chiral light, which carries spin angular momentum and orbital angular momentum (OAM)¹², the latter characterized by a helical phase $\exp(i\ell\phi)$ about the azimuth (ϕ) with helicity ℓ . Driven by the many applications these beams have spurred¹³, much attention has been focused on their efficient creation.

Scalar OAM modes are easily created by dynamic phase approaches¹⁴, while geometric phase is a convenient mechanism for creating vector combinations of spin and OAM^{15–21}, forming cylindrical vector vortex beams that are rotationally symmetric complex states of light with an internal intensity null due to a polarization singularity²². They are conveniently expressed on the higher-order Poincaré sphere (HOPS)^{23,24}, where the poles are combinations of left- and right-circular spin angular momentum states ($\pm\sigma$) combined with symmetrical left- and right-helicity OAM states ($\pm\ell$). This vector addition has opened many exciting possibilities for new applications that exploit chiral control of both spin angular momentum and OAM degrees of freedom of light^{25–27}.

An ongoing challenge is to control light's chirality, spin and orbital at source^{28–31}. So far, advances have been limited, in part due to fundamental symmetry restrictions when using geometric phase and topological photonics and in part due to implementation restrictions, for example, in regard to the physical size and spatial resolution of the optical elements. Such advances include the generation of symmetric OAM states via the geometric phase^{32,33}, as integrated on-chip devices^{34–40}, in organic lasers⁴¹ and as fibre lasers⁴². Despite these impressive advances, breaking the symmetry of the spin and orbital states for arbitrary angular momentum control of light

at source has remained elusive. Arbitrary angular momentum control requires the ability to produce any desired spin-orbital chiral state of light, including arbitrary, differing and non-symmetric OAM values coupled to user-defined polarizations, an infinitely larger set than the special case of symmetric OAM states, allowing access to super-chiral light with high angular momentum. In contrast, OAM lasers so far have been demonstrated with only symmetric superpositions of $\pm\ell$ and $\pm\sigma$, which add to a total angular momentum of zero, and with modest OAM values of up to $|\ell|=\pm 10$ (ref. 32). However, super-chiral light with high angular momentum is known to be important in many fundamental and applied studies, for example, in quantum studies with Bose-Einstein condensates, remote sensing with structured light, accurate rotation measurements, metrology of chiral media and for larger photon information capacity⁴³.

Here, we report a laser with an intracavity metasurface for control of light's angular momentum at source. We design custom metasurfaces for arbitrary OAM coupling to linear polarization states, including a metasurface with an extreme imbedded helicity of up to $\ell=100$. By doing so, we are able to produce new chiral states of light from a laser, including simultaneous lasing across vastly differing and non-symmetric OAM values that are up to $\Delta\ell=90$ apart, an extreme violation of previous symmetric spin-orbit (SO) lasing devices, and demonstrate some intriguing lasing phenomena, for example, vortex splitting inside a laser medium and coherent lasing across modes with no spatial overlap. By designing a cavity for mode metamorphosis, our laser is able to generate ultrahigh-purity OAM modes with orders of magnitude enhanced purity over their externally created counterparts, which we show with OAM modes up to $\ell=100$. Importantly, the coupling to linear polarization states facilitates a compact design with a reduction in complexity and number of optical elements over previous geometric phase lasers, the latter of course restricted to only symmetric states. In addition to these

¹School of Physics, University of the Witwatersrand, Wits, South Africa. ²Harvard John A. Paulson School of Engineering and Applied Sciences, Harvard University, Cambridge, MA, USA. ³Department of Electrical and Computer Engineering, National University of Singapore, Singapore, Singapore. ⁴CSIR National Laser Centre, Pretoria, South Africa. ⁵Applied Physics, Vrije Universiteit Brussel, Brussels, Belgium. ⁶Center for Nanoscale Systems, Harvard University, Cambridge, MA, USA. ⁷CNST - Fondazione Istituto Italiano di Tecnologia Via Giovanni Pascoli, Milan, Italy. ⁸Present address: Molecular Chirality Research Center, Chiba University, Inage-ku, Chiba, Japan. ✉e-mail: andrew.forbes@wits.ac.za

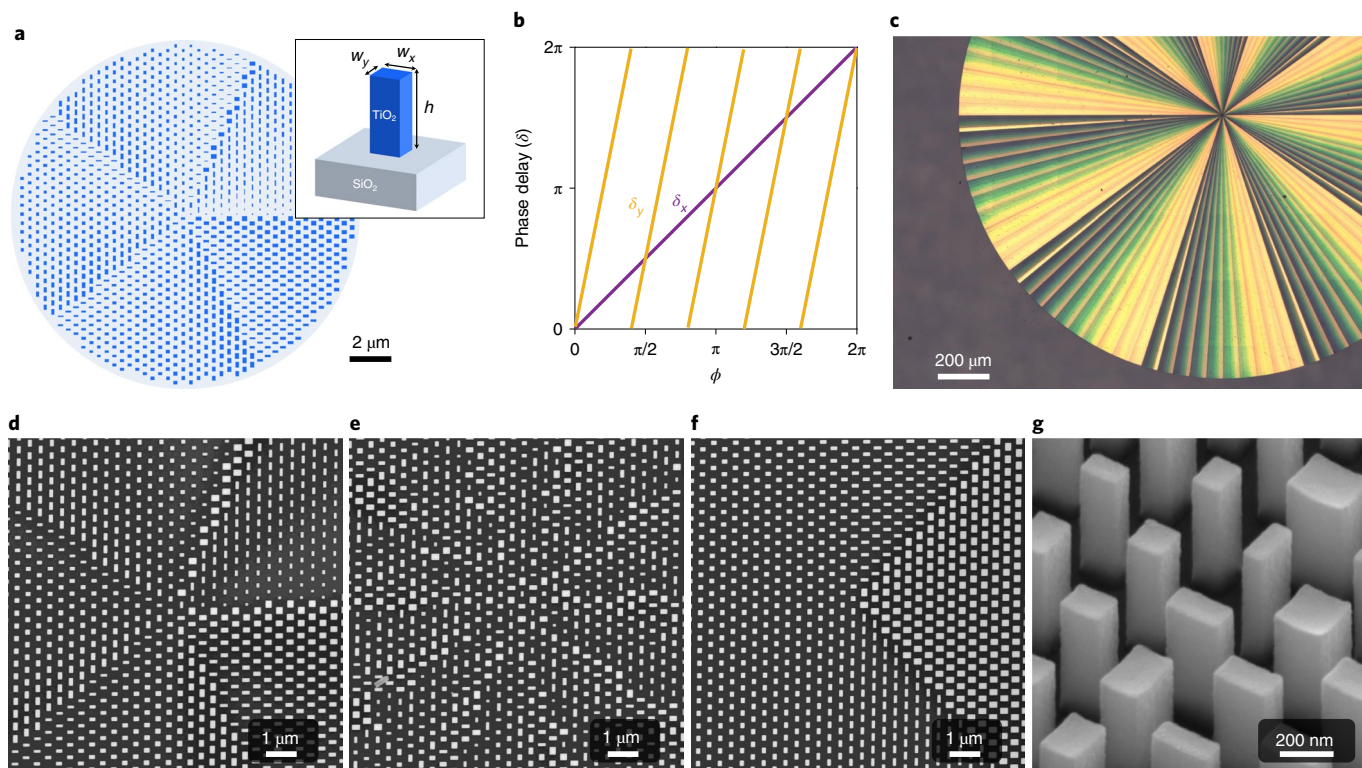


Fig. 1 | Metasurface design and characterization. **a**, Schematic of the central part of our metasurface, which imprints two kinds of helical phase profiles for x - and y -incident polarization, resulting in output beams with OAM of $\ell_1 h$ and $\ell_2 h$. The metasurface elements are rectangular nanopillars made of amorphous TiO_2 with fixed height, $h = 600$ nm. By changing the width along the x and y directions, the nanoposts impart azimuthal phase delays given by δ_x and δ_y . **b**, Required phase delays for output beam OAM values of $\ell_1 = 1$ and $\ell_2 = 5$ (JP2). **c**, Optical micrograph of JP3 with OAM values of $\ell_1 = 10$ and $\ell_2 = 100$. **d-f**, Scanning electron micrographs of the central parts of JP1 (**d**), JP2 (**e**) and JP3 (**f**). **g**, Tilted scanning electron micrograph showing the nanoposts of JP2. All our J-plates were fabricated using the process detailed in ref. ⁴⁵.

advances, our laser conveniently operates in the visible, produces all previous observed OAM states from lasers, while our metasurface fabrication facilitates high damage threshold operation.

Results

Metasurface J-plates. In this work we design and fabricate metasurfaces to engineer a compact visible metasurface laser for general states of super-chiral light. Our SO device, which we call a J-plate, is a dielectric metasurface made of amorphous TiO_2 nanoposts (with rectangular section) on a fused-silica substrate (Fig. 1a). Each post has a height of 600 nm, while the width and length (W_x , W_y) change so as to impart a different phase delay to the propagating visible light at a wavelength of 532 nm. More specifically, the J-plate can impart different azimuthal phase delays δ_x and δ_y on the field polarization components (horizontal and vertical) (Fig. 1b).

In the past, devices based on both liquid crystals and metasurfaces have been proposed that use the Pancharatnam-Berry (PB) phase to impart OAM to circularly polarized beams. In this case, all the elements of the device, either liquid-crystal molecules or nanoposts, are the same but azimuthally oriented to impose a helical wavefront to the propagating light. In such devices, the $\pm h$ spin momentum of the incident light is converted into the opposite spin (opposite polarization handedness) and $\pm \ell h$ of OAM (while an opposite angular momentum is transferred to the device itself). The angular momentum of each component therefore cancels for zero net angular momentum. Lasers based on this concept have been demonstrated using liquid crystals with up to $\ell = \pm 10$ (ref. ³²) and metasurfaces up to $\ell = \pm 3$ (ref. ³³), and similar concepts have been exploited for on-chip control of scalar OAM up to $\ell = \pm 2$ (ref. ³⁶).

Table 1 | Three metasurface designs (JP1, JP2 and JP3) for arbitrary angular momentum control from our laser

Incident state	$ H, \ell = 0\rangle$	$ V, \ell = 0\rangle$
JP1	$ H, \ell = -1\rangle$	$ V, \ell = 1\rangle$
JP2	$ H, \ell = 1\rangle$	$ V, \ell = 5\rangle$
JP3	$ H, \ell = 10\rangle$	$ V, \ell = 100\rangle$

The incident scalar Gaussian states are converted into arbitrary vector OAM states.

Our metasurface is more general than these devices and is designed to convert any two orthogonal polarization states of the incident light into helical modes with any arbitrary value of OAM, ℓ_1 and ℓ_2 , and not just opposite values. This is possible by controlling the PB phase, the overall phase and the form birefringence of each element^{44,45}. We designed and fabricated three such elements, JP1, JP2 and JP3, with the SO coupling described in Table 1. JP1 allows us to replicate previous SO lasers that produce only symmetric states, that is, $\ell_1 = -\ell_2$ (the linear polarization can be flipped with a quarter-waveplate to produce cylindrical vector vortex beams; see Supplementary Information) while JP2 and JP3 allow for the most general OAM states to be produced from a laser.

Figure 1c presents an optical microscope image of JP3, which produces helical modes with OAM of $\ell = 10$ and $\ell = 100$ for horizontally and vertically polarized incident light, respectively. The implemented azimuthal phase gradient is visible in the optical image of the device as a colour variation (nanoposts with different

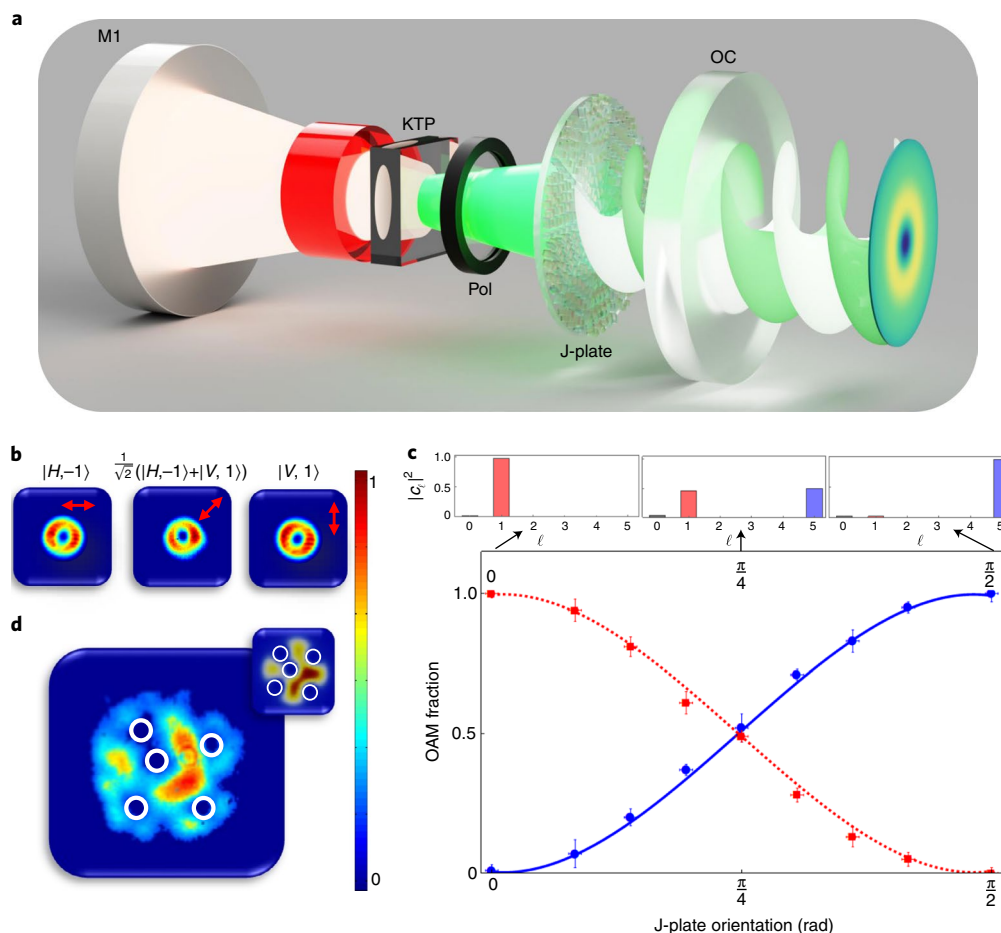


Fig. 2 | Metasurface laser and modes. **a**, Illustration of laser cavity with an intracavity nonlinear crystal (KTP), polarizer (Pol) and metasurface (J-plate), excited by an infrared pump (between mirror M1 and the back KTP crystal face), with the green light emerging from the output coupler (OC) mirror. **b**, Replication of previous SO laser results showing symmetric states of $|\ell| = \pm 1$ for three orientations of the fast axis of JP1 (red arrows). **c**, Creation of a new angular momentum state with $\ell_1 = 1$ and $\ell_2 = 5$. As θ (J-plate orientation) is varied, the modal spectrum shifts from $|H, 1\rangle$ (red squares) to $|V, 5\rangle$ (blue circles), in agreement with theory (curves). Insets: the OAM spectrum at different θ . Error bars show standard deviations. **d**, Creation of an arbitrary vector superposition state of coherently mixed vortices showing five distinct phase singularities (indicated by white circles), in agreement with theory (shown in the inset). All results were taken at an average pump energy of 230 mJ. For **b** and **d**, the colour bar shows normalized intensity plotted with a false colour scale of 0 to 1.

shapes have different scattering resonance frequencies, resulting in a colourful optical image). Note that it is easy to distinguish 10 sectors, each made of 10 inner sectors. This means that, for the helical mode resulting from incident vertically polarized light, to generate a beam with OAM $\ell = 100$, a 2π azimuthal phase variation must be accumulated in an angle of just $2\pi/100$. Such a high phase gradient has never been implemented into any metasurface before. Figure 1d–f presents scanning electron microscopy (SEM) images of the metasurface devices summarized in Table 1 (from left to right: JP1, JP2 and JP3, respectively): the nanoposts have different shapes and orientations to implement the necessary phase gradient by combining the propagation phase, PB phase and form birefringence as described earlier. This is visualized in Fig. 1g, which shows a tilted SEM image of a few typical nanoposts constituting one of our devices.

Intracavity implementation. Our laser, shown schematically in Fig. 2a, was constructed as a frequency-doubled cavity that converts the infrared fundamental frequency of Nd:YAG ($\lambda = 1,064$ nm) to the second-harmonic green ($\lambda = 532$ nm) through an intracavity nonlinear crystal (KTP). The J-plate was placed in the resonant green cavity to provide a geometry that represents the first visible

metasurface-assisted laser. We will refer to this geometry as our ‘metasurface laser’.

The concept of the laser design exploits a unique feature of our metasurfaces, namely OAM coupling to linear polarization states. The resonant mode morphs from a linearly polarized Gaussian-like enveloped beam at one end of the cavity to an arbitrary angular momentum state at the other. Although a polarizer was required for selection of the horizontal polarization state before the J-plate, the polarization of the light traversing the J-plate was controlled by simply rotating the J-plate itself. This relative rotation can be viewed as the alignment of the polarization state to the optical fast axis of the J-plate.

The intracavity light undergoes multiple passes backwards and forwards through the metasurface (see Supplementary Information and Supplementary Video 1). Starting as $|H, 0\rangle$ (horizontally polarized and no OAM), it is converted to the desired combination within the laser, say $\cos\theta|H, \ell_1\rangle + \sin\theta|V, \ell_2\rangle$ (where θ is the angle of the fast axis of the J-plate with respect to the horizontal), the most general OAM state possible and a state never previously created from a laser cavity. As the SO effect couples OAM to linear polarization states, mirror reflections do not result in any spin flipping, and only the OAM handedness changes sign; conventional

SO coupling lasers flip both the spin and OAM, which prohibits a simple two-mirror cavity (see Supplementary Information). The present design thus leads to a reduction in the number of optical elements and the cavity complexity compared with previous designs. On reflection from the output coupler mirror back to the J-plate, the state is $\cos\theta|H, -\ell_1\rangle + \sin\theta|V, -\ell_2\rangle$. From the reciprocity of the metasurface, the initial state $|H, 0\rangle$ is regained, which then returns through the polarizer to the KTP crystal. Ordinarily, vastly differing ℓ modes would occupy different crystal gain regions and therefore would lase independently; in our design, the modes overlap within the crystal, ensuring spatial coherence even without any spatial overlap at the output. The state $\cos\theta|H, \ell_1\rangle + \sin\theta|V, \ell_2\rangle$ is then a repeating mode after each round trip and thus full angular momentum control from the laser is possible.

Generation of symmetric OAM and HOPS states. We first replicate previous geometric phase lasers by creating linear HOPS beams with conjugate OAM states, that is $|\ell_1| = -|\ell_2|$. Figure 2b presents example output modes at different angles (shown as inset red arrows) of the JP1 metasurface. As expected, the output modes are annular-shaped intensity profiles that remain invariant during rotation of the metasurface (all states on the HOPS have the same intensity profile) while modal analysis confirmed the expected OAM structure (see Supplementary Information).

Arbitrary angular momentum control. To demonstrate arbitrary angular momentum control we used JP2 to create laser modes with asymmetric OAM states described by $\cos\theta|H, 1\rangle + \sin\theta|V, 5\rangle$. As JP2 is rotated, the output mode shifts in weighting from an OAM of $\ell_1 = 1$ to an OAM of $\ell_2 = 5$, with arbitrary vector superpositions in between (shown in Fig. 2c, with insets showing the measured OAM spectrum at the different rotation angles). At intermediate JP2 rotations a superposition of the two OAM modes is present, including the special case of an equal OAM fraction. When added coherently, the prediction is a non-trivial superposition of vortices with a central vortex of charge ℓ_1 surrounded by $|\ell_1 - \ell_2|$ single-charged peripheral vortices of sign $\ell_2/|\ell_2|$ (ref. 46). In our case, this translates to a central vortex of charge +1 with four surrounding vortices of charge +1 (the sum does not add to 6, contrary to what one might have expected). This was observed experimentally and is shown in Fig. 2d (the inset shows the theoretical prediction). The singularities are highlighted by white circles. This demonstrates that our laser can not only reproduce all previous SO results with a simpler cavity configuration, but is also able to produce more exotic states of light.

Having demonstrated arbitrary angular momentum control within a laser, we now demonstrate extreme SO asymmetric coupling using JP3 in a metasurface laser for an output state of $\cos\theta|H, 10\rangle + \sin\theta|V, 100\rangle$. Here, the difference in helicity is $\Delta\ell = |\ell_1 - \ell_2| = 90$. The successful generation of this general OAM state is shown in Fig. 3. As the weighting of the states is altered through JP3 rotation (control of θ), the superposition state changes from $|H, 10\rangle$ on one pole to $|V, 100\rangle$ on the other. Intermediate states show the progression from lasing on one mode to the other: contrary to the previous asymmetric case ($\ell_1 = 1$ and $\ell_2 = 5$), here the composite-vortex beams are found to possess a structure that contains two superimposed concentric rings. This can be understood as $\ell_1 \ll \ell_2$, and thus each state is simultaneously lasing but occupying completely different spatial regions after the metasurface (but overlapping in the crystal for coherence).

Modal purity. In Fig. 4 we compare the purity of the OAM laser modes (blue) to the corresponding externally generated modes with the same J-plate (red) for $\ell = 10$ and $\ell = 100$ using modal decomposition, allowing the modal power contribution to each mode in the Laguerre–Gaussian (LG) basis to be measured and calculated (see Supplementary Information). The LG basis has both azimuthal (ℓ)

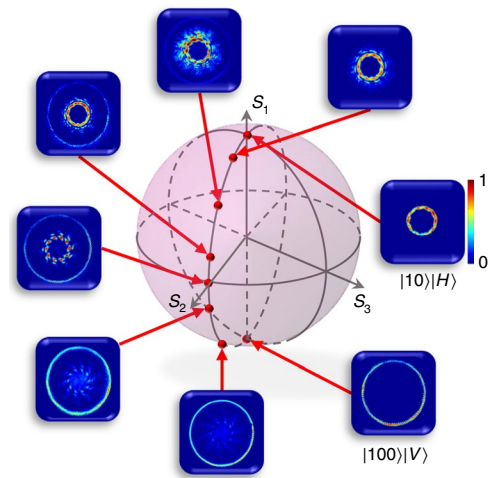


Fig. 3 | Extreme SO lasing. Various measured states from the laser, displayed on a generalized OAM sphere. Here, the poles are asymmetric with OAM order $\ell_1 = 10$ (north pole) and $\ell_2 = 100$ (south pole). The transition from one to the other allows visualization of lasing across vastly differing OAM values as superpositions with two concentric rings. The operating pump energy was 315 mJ. The colour bar shows normalized intensity plotted with a false colour scale of 0 to 1.

and radial (p) terms, the former responsible for the OAM content. Ideally, a pure OAM mode would have high power content in the desired ℓ and $p = 0$ mode. Figure 4a reports the results for $\ell = 10$ modes: we see that generation of the modes from inside the laser cavity yields a high OAM purity of 92% (compared to only 72% for external generation using the same metasurface). More telling is the fact that the 92% is contained entirely in the desired $p = 0$ mode, whereas the 72% for external generation is spread across numerous radial modes. The bottom panel of Fig. 4a shows a more detailed view, with the measured and calculated radial mode expansion, confirming that the laser produces ultrahigh-purity OAM modes in comparison to externally generated modes (the interesting damped oscillatory nature of the p -mode weightings is predicted by theory; see Supplementary Information). This is echoed in the beam structures shown in Fig. 4b,c for the internally and externally generated modes, respectively, with the former showing the telltale signs of a radial ring structure rather than the single ring of the desired vortex state.

This external purity degradation becomes more pronounced at higher OAM values⁴⁷. In Fig. 4d,e we show the $\ell = 100$ externally generated mode and the laser mode, respectively. The visual effect is striking: distinct spatial ring structures and a radial outward spread in intensity can be observed in the externally generated mode, compared to the well-defined annular ring structure for the laser generated mode. For the $\ell = 100$ mode shown in Fig. 4d, the experimentally measured 71% OAM purity has only ~13% (Supplementary Table I) in the desired $\ell = 100$, $p = 0$ mode, while the laser mode shown in Fig. 4e has a purity of ~90% in the $p = 0$ mode. This is shown quantitatively in Fig. 4f, with the OAM mode spectrum shown for the laser mode (blue bars) and the externally created mode (red lollipop). There is a slight decrease in purity relative to the $\ell = 10$ mode, but the purity remains very high.

In our comparative analysis, all decompositions of the laser generated modes were performed at a common scale of w_0 (the embedded Gaussian radius), while the scale for the external modes was optimally adjusted for each mode to $w_{\text{opt}} = w_0 / \sqrt{|\ell| + 1}$, an optimal scale to maximize the power content of the $p = 0$ mode. Figure 4g shows a comparison of the laser mode purity measured at the scale w_0 versus the external generated beams measured at the

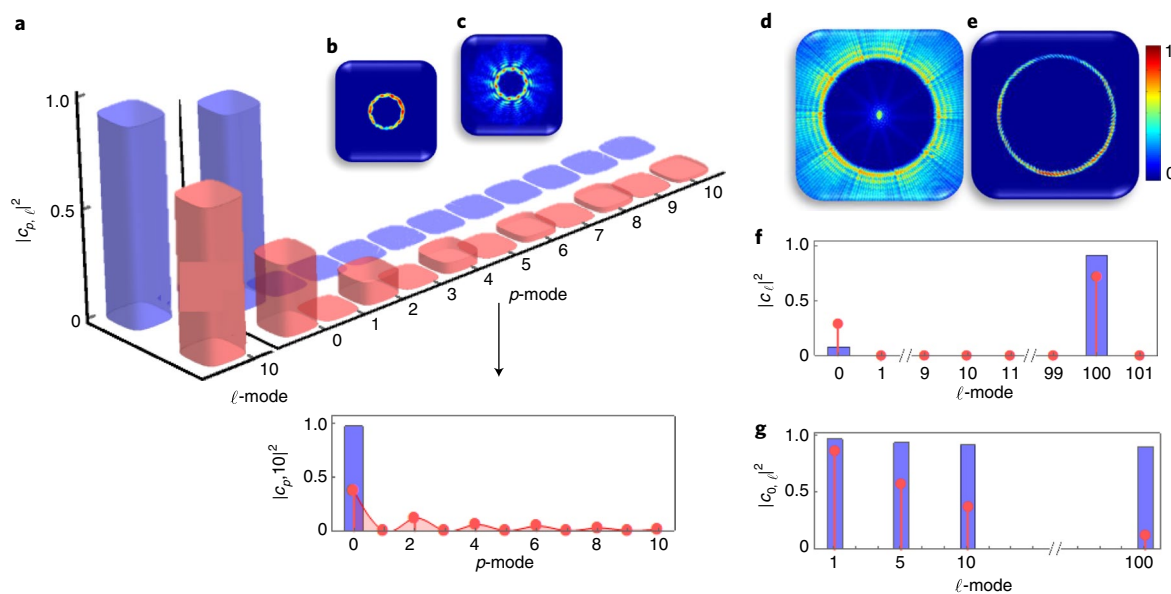


Fig. 4 | Ultrapure OAM lasing modes. **a**, Measured modal spectrum for $\ell=10$, both internal (blue) and external (red) to the laser. $|c_{p,\ell}|^2$ is the modal power in the p th radial mode and ℓ th OAM mode. **b, c**, The corresponding beam intensities are shown for the internal modes (**b**) and external modes (**c**). The bottom inset in **a** shows an enlarged version with experimental data (lollipop bars) and theoretical predictions (solid line). **d, e**, The same analysis, performed on the $\ell=100$ modes, showing intensity profiles created external (**d**) and internal (**e**) to the laser. The colour bar shows normalized intensity plotted with a false colour scale of 0 to 1. **f**, OAM distribution of external (red lollipops) and laser (blue bars) modes, where $|c_{\ell}|^2$ represents the total OAM modal power (summed over all p modes). **g**, Comparison of the $p=0$ mode weightings for the externally generated beams (red lollipops) versus cavity modes (blue bars). The operating pump energy was 315 mJ for all measurements.

scale w_{opt} for all modes generated in this study (see Supplementary Table I for full measurement values). Although the scale for the external beam decomposition changes drastically across the ℓ spectrum, our laser produces much higher purity for all ℓ at the same intuitive scale, w_0 .

There are several mechanisms that give rise to this enhanced purity. Recall that, external to the laser, the radial modes appear because of a missing amplitude term; in the laser the lowest loss mode has the required amplitude by cavity diffraction, while the radial modes that are created are suppressed. For example, diffraction results in a resonant mode that has a Gaussian-like envelope (but is not Gaussian) at the KTP crystal for all OAM modes, while the output OAM scale is fixed by the radius of curvature of the output mirror and the cavity length. The resonant mode inside the cavity differs from plane to plane: at the plane of the J-plate it has the required (missing) amplitude term to produce a high-purity LG $p=0$ at the output coupler. Furthermore, the multiple passes in the green cavity ensure radial mode suppression by gain-assisted filtering, by virtue of the overlap of the resonant mode and the infrared pump mode. The radial modes are similarly suppressed by the mode-dependent resonant frequencies of the cavity, enhanced further by the limited excitation of radial modes through nonlinear modal coupling inside the crystal⁴⁸. Together then, the cavity suppresses radial modes by a combination of diffraction-induced filtering, resonance-induced filtering and gain-assisted filtering. All these mechanisms prevail to allow high-purity OAM lasing.

Discussion and conclusion

The concept of the laser exploits our metasurface's extraordinary feature of coupling arbitrary OAM to arbitrary spin states, which we have demonstrated with OAM up to $\ell=100$ and with a large OAM differential between modes of up to $\Delta\ell=90$, representing intracavity SO symmetry-breaking for super-chiral light. The metasurface approach has the additional benefits of a high damage

threshold⁴⁹ and spatial resolution down to the nanometre scale for a well-defined singularity with low loss. Our approach has allowed the demonstration of an order-of-magnitude higher OAM than previously reported from geometric phase lasers, a high total angular momentum in our vector states (symmetric lasers have zero total angular momentum), all in ultrahigh-purity modes in the visible.

What we find particularly exciting is that our approach lends itself to many laser architectures. For example, one could increase the gain volume and metasurface size to produce a bulk laser for high power or one could shrink the system down to a microchip using a monolithic metasurface design. Although we have controlled the intracavity polarization and rotated the J-plate for mode control, the lasing mode could be controlled by manipulating the polarization of the pump beam with a judiciously chosen nonlinear crystal⁵⁰ for a dynamically switchable laser output. Thus, our work represents an important step towards merging the research in bulk OAM lasers and that of on-chip devices.

In summary, we have demonstrated a laser that produces all OAM states previously observed from lasers as well as new forms of chiral light not observed from lasers until now. The demonstrated performance, versatility in design and power-handling capabilities of our approach point to an exciting route to control light's angular momentum at the source.

Online content

Any methods, additional references, Nature Research reporting summaries, source data, extended data, supplementary information, acknowledgements, peer review information; details of author contributions and competing interests; and statements of data and code availability are available at <https://doi.org/10.1038/s41566-020-0623-z>.

Received: 25 April 2019; Accepted: 18 March 2020;
Published online: 27 April 2020

References

1. Rubinsztein-Dunlop, H. et al. Roadmap on structured light. *J. Opt.* **19**, 013001 (2016).
2. Willner, A. E. et al. Optical communications using orbital angular momentum beams. *Adv. Opt. Photon.* **7**, 66–106 (2015).
3. Wang, J. Advances in communications using optical vortices. *Photon. Res.* **4**, B14–B28 (2016).
4. Wang, J. Data information transfer using complex optical fields: a review and perspective. *Chin. Opt. Lett.* **15**, 030005 (2017).
5. Ndagano, B., Nape, I., Cox, M. A., Rosales-Guzman, C. & Forbes, A. Creation and detection of vector vortex modes for classical and quantum communication. *J. Lightw. Technol.* **36**, 292–301 (2018).
6. Krenn, M., Malik, M., Erhard, M. & Zeilinger, A. Orbital angular momentum of photons and the entanglement of Laguerre–Gaussian modes. *Philos. Trans. R. Soc. A* **375**, 20150442 (2017).
7. Erhard, M., Fickler, R., Krenn, M. & Zeilinger, A. Twisted photons: new quantum perspectives in high dimensions. *Light Sci. Appl.* **7**, 17111–17146 (2018).
8. Moreau, P. A., Toninelli, E., Gregory, T. & Padgett, M. J. Ghost imaging using optical correlations. *Laser Photon. Rev.* **12**, 1700143 (2018).
9. Maurer, C., Jesacher, A., Bernet, S. & Ritsch-Marte, M. What spatial light modulators can do for optical microscopy. *Laser Photon. Rev.* **5**, 81–101 (2011).
10. Grier, D. G. A revolution in optical manipulation. *Nature* **424**, 810–816 (2003).
11. Padgett, M. J. & Bowman, R. Tweezers with a twist. *Nat. Photon.* **5**, 343–348 (2011).
12. Allen, L., Beijersbergen, M. W., Spreeuw, R. J. C. & Woerdman, J. P. Orbital angular momentum of light and the transformation of Laguerre–Gaussian laser modes. *Phys. Rev. A* **45**, 8185–8189 (1992).
13. Padgett, M. J. Orbital angular momentum 25 years on. *Opt. Express* **25**, 11265–11274 (2017).
14. Heckenberg, N., McDuff, R., Smith, C. & White, A. Generation of optical phase singularities by computer-generated holograms. *Opt. Lett.* **17**, 221–223 (1992).
15. Marrucci, L., Manzo, C. & Paparo, D. Optical spin-to-orbital angular momentum conversion in inhomogeneous anisotropic media. *Phys. Rev. Lett.* **96**, 163905 (2006).
16. Brasselet, E., Murazawa, N., Misawa, H. & Juodkazis, S. Optical vortices from liquid crystal droplets. *Phys. Rev. Lett.* **103**, 103903 (2009).
17. Brasselet, E. Tunable high-resolution macroscopic self-engineered geometric phase optical elements. *Phys. Rev. Lett.* **121**, 033901 (2018).
18. Nassiri, M. G. & Brasselet, E. Multispectral management of the photon orbital angular momentum. *Phys. Rev. Lett.* **121**, 213901 (2018).
19. Nersisyan, S. R., Tabiryan, N. V., Steeves, D. M. & Kimball, B. R. The promise of diffractive waveplates. *Opt. Photon. News* **21**, 40–45 (2010).
20. Rubano, A., Cardano, F., Piccirillo, B. & Marrucci, L. Q-plate technology: a progress review. *J. Opt. Soc. Am. B* **36**, D70–D87 (2019).
21. Piccirillo, B., Slussarenko, S., Marrucci, L. & Santamato, E. The orbital angular momentum of light: genesis and evolution of the concept and of the associated photonic technology. *Riv. Nuovo Cimento* **36**, 501–555 (2013).
22. Zhan, Q. Cylindrical vector beams: from mathematical concepts to applications. *Adv. Opt. Photon.* **1**, 1–57 (2009).
23. Milione, G., Sztul, H., Nolan, D. & Alfano, R. Higher-order Poincaré sphere, Stokes parameters, and the angular momentum of light. *Phys. Rev. Lett.* **107**, 053601 (2011).
24. Holleczek, A., Aiello, A., Gabriel, C., Marquardt, C. & Leuchs, G. Classical and quantum properties of cylindrically polarized states of light. *Opt. Express* **19**, 9714–9736 (2011).
25. Rosales-Guzmán, C., Ndagano, B. & Forbes, A. A review of complex vector light fields and their applications. *J. Opt.* **20**, 123001 (2018).
26. Cardano, F. & Marrucci, L. Spin-orbit photonics. *Nat. Photon.* **9**, 776–778 (2015).
27. Otte, E., Alpmann, C. & Denz, C. Polarization singularity explosions in tailored light fields. *Laser Photon. Rev.* **12**, 1700200 (2018).
28. Forbes, A. Controlling light's helicity at the source: orbital angular momentum states from lasers. *Philos. Trans. R. Soc. A* **375**, 20150436 (2017).
29. Omatsu, T., Miyamoto, K. & Lee, A. J. Wavelength-versatile optical vortex lasers. *J. Opt.* **19**, 123002 (2017).
30. Wang, X. et al. Recent advances on optical vortex generation. *Nanophotonics* **7**, 1533–1556 (2018).
31. Forbes, A. Structured light from lasers. *Laser Photon. Rev.* **13**, 1900140 (2019).
32. Naidoo, D. et al. Controlled generation of higher-order Poincaré sphere beams from a laser. *Nat. Photon.* **10**, 327–332 (2016).
33. Maguid, E. et al. Topologically controlled intracavity laser modes based on Pancharatnam–Berry phase. *ACS Photonics* **5**, 1817–1821 (2018).
34. Cai, X. et al. Integrated compact optical vortex beam emitters. *Science* **338**, 363–366 (2012).
35. Miao, P. et al. Orbital angular momentum microlaser. *Science* **353**, 464–467 (2016).
36. Zambon, N. C. et al. Optically controlling the emission chirality of microlasers. *Nat. Photon.* **13**, 283–288 (2019).
37. Li, H. et al. Orbital angular momentum vertical-cavity surface-emitting lasers. *Optica* **2**, 547–552 (2015).
38. Xie, Z. et al. Ultra-broadband on-chip twisted light emitter for optical communications. *Light Sci. Appl.* **7**, 18001 (2018).
39. Hayenga, W. E. et al. Direct generation of tunable orbital angular momentum beams in microring lasers with broadband exceptional points. *ACS Photonics* **6**, 1895–1901 (2019).
40. Seghilani, M. S. et al. Vortex laser based on III–V semiconductor metasurface: direct generation of coherent Laguerre–Gauss modes carrying controlled orbital angular momentum. *Sci. Rep.* **6**, 38156 (2016).
41. Stellinga, D. et al. An organic vortex laser. *ACS Nano* **12**, 2389–2394 (2018).
42. Mao, D. et al. Ultrafast all-fiber based cylindrical-vector beam laser. *Appl. Phys. Lett.* **110**, 021107 (2017).
43. Yao, A. M. & Padgett, M. J. Orbital angular momentum: origins, behavior and applications. *Adv. Opt. Photon.* **3**, 161–204 (2011).
44. Devlin, R. C., Ambrosio, A., Rubin, N. A., Mueller, J. B. & Capasso, F. Arbitrary spin-to-orbital angular momentum conversion of light. *Science* **358**, 896–901 (2017).
45. Devlin, R. C. et al. Spin-to-orbital angular momentum conversion in dielectric metasurfaces. *Opt. Express* **25**, 377–393 (2017).
46. Baumann, S., Kalb, D., MacMillan, L. & Galvez, E. Propagation dynamics of optical vortices due to Gouy phase. *Opt. Express* **17**, 9818–9827 (2009).
47. Sephton, B., Dudley, A. & Forbes, A. Revealing the radial modes in vortex beams. *Appl. Opt.* **55**, 7830–7835 (2016).
48. Schwob, C. et al. Transverse effects and mode couplings in OPOS. *Appl. Phys. B* **66**, 685–699 (1998).
49. Yao, J. et al. Investigation of damage threshold to TiO₂ coatings at different laser wavelength and pulse duration. *Thin Solid Films* **516**, 1237–1241 (2008).
50. Taira, T., Sasaki, T. & Kobayashi, T. Polarization control of Q-switch solid-state lasers with intracavity SHG crystals. *Electron. Commun. Jpn* **2** **75**, 1–12 (1992).

Publisher's note Springer Nature remains neutral with regard to jurisdictional claims in published maps and institutional affiliations.

© The Author(s), under exclusive licence to Springer Nature Limited 2020

Methods

Our metasurface laser comprised a nonlinear crystal inside its own cavity, which itself was placed inside an infrared cavity, to achieve a resonant optical parametric oscillator configuration. The infrared gain medium was a 1.1% doped Nd:YAG crystal rod with dimensions of 76 mm (length) by 6.35 mm (diameter). The crystal was flash-lamp side-pumped. For second-harmonic generation, a nonlinear KTP crystal (type 0, $3 \times 3 \times 5 \text{ mm}^3$) was used to convert the intracavity infrared light ($\lambda = 1,064 \text{ nm}$) of the Nd:YAG to second-harmonic green light at $\lambda = 532 \text{ nm}$. The input face of the KTP crystal was antireflection-coated for $\lambda = 1,064 \text{ nm}$ and high-reflection-coated for $\lambda = 532 \text{ nm}$, while the output face was highly transmissive at the second-harmonic wavelength ($\lambda = 532 \text{ nm}$) and was high-reflection-coated at $\lambda = 1,064 \text{ nm}$. The back reflector mirror M1 was a concave mirror with radius of curvature (ROC) of 400 mm and had a reflectivity of 98%, whereas the output coupler mirror (ROC = 200 mm) was highly reflective at $\lambda = 1,064 \text{ nm}$ while coupling 0.8% of the intracavity green light outside the cavity. The KTP crystal was placed at the infrared beam waist position while the J-plate was placed adjacent to the output coupler mirror. Both theory and experiment have shown that the cavity length is far more critical than the position of the J-plate inside the cavity. This can be understood from the fact that the mode discrimination is dependent on the size of the resonant mode at the crystal and the resonant frequencies, both influenced by cavity length, whereas the position of the J-plate merely impacts the spectrum of modes created, finally to be removed by the cavity after many round trips by the discrimination process. The resonant mirrors were spaced by an effective distance of $\sim 600 \text{ mm}$. The empty (with no J-plate) cavity length was adjusted so that the spot size of the $\lambda = 1,064 \text{ nm}$ beam at the crystal input surface was measured to be $81 \mu\text{m}$ (close to the calculated value of $82.3 \mu\text{m}$), while the spot size of the output green beam was $62 \mu\text{m}$ (close to the calculated value of $64.4 \mu\text{m}$) at the KTP crystal. This ensured that the green cavity would have excellent gain overlap for only low radial modes. The laser was gain-switched with the $\lambda = 1,064 \text{ nm}$ output pulse duration of 40 ns. The conversion efficiency of the KTP was 18% under the single-pass configuration and increased to $\sim 61\%$ once the output coupler mirror was in place to form the green resonant cavity. The isolation of the $\lambda = 532 \text{ nm}$ output from the cavity output coupler mirror was confirmed by measuring the emission spectra of the output (see Supplementary Information) using a spectrometer (Ocean Optics). We quantitatively confirmed the advantages of our intracavity approach versus an equivalent extracavity generation approach using the modal decomposition technique. The output beam was directed toward a spatial light modulator, which was digitally encoded with a match filter in the LG basis. The resultant field was transformed in the Fourier plane using a Fourier lens ($f = 300 \text{ mm}$), which was positioned a focal length from the plane of the spatial light modulator. The on-axis

intensities at the Fourier plane after the lens were recorded using a charge-coupled device camera. After subtracting any noise from the system, the modal weightings were evaluated by normalizing the on-axis intensities.

Data availability

The data that support the plots within this paper and other findings of this study are available from the corresponding author upon reasonable request.

Code availability

The codes that support the plots and multimedia files within this paper are available from the corresponding author upon reasonable request.

Acknowledgements

A.V. acknowledges support from the Claude Leon Foundation. This work was performed, in part, at the Center for Nanoscale Systems (CNS), a member of the National Nanotechnology Coordinated Infrastructure (NNCI), which is supported by the NSF under award no. 1541959. CNS is a part of Harvard University. F.C. is supported by funding from the Air Force Office of Scientific Research (grant nos. MURI: FA9550-14-1-0389, FA9550-16-1-0156), and the King Abdullah University of Science and Technology (KAUST) Office of Sponsored Research (OSR) (award no. OSR-2016-CRG5-2995). Y.-W.H. and C.-W.Q. are supported by the National Research Foundation, Prime Minister's Office, Singapore under its Competitive Research Program (CRP award no. NRF-CRP15-2015-03).

Author contributions

H.S., D.N., B.S. and A.V. performed experiments with custom optics designed and fabricated by Y.-W.H. and A.A. All authors contributed to data analysis and writing of the manuscript. A.F., F.C. and C.-W.Q. supervised the project.

Competing interests

The authors declare no competing interests.

Additional information

Supplementary information is available for this paper at <https://doi.org/10.1038/s41566-020-0623-z>.

Correspondence and requests for materials should be addressed to A.F.

Reprints and permissions information is available at www.nature.com/reprints.

In the format provided by the authors and unedited.

High-purity orbital angular momentum states from a visible metasurface laser

Hend Sroor¹, Yao-Wei Huang^{2,3}, Bereneice Sephton¹, Darryl Naidoo^{1,4}, Adam Vallés^{1,8}, Vincent Ginis^{2,5}, Cheng-Wei Qiu³, Antonio Ambrosio^{6,7}, Federico Capasso^{1,2} and Andrew Forbes¹✉

¹School of Physics, University of the Witwatersrand, Wits, South Africa. ²Harvard John A. Paulson School of Engineering and Applied Sciences, Harvard University, Cambridge, MA, USA. ³Department of Electrical and Computer Engineering, National University of Singapore, Singapore, Singapore. ⁴CSIR National Laser Centre, Pretoria, South Africa. ⁵Applied Physics, Vrije Universiteit Brussel, Brussels, Belgium. ⁶Center for Nanoscale Systems, Harvard University, Cambridge, MA, USA. ⁷CNST – Fondazione Istituto Italiano di Tecnologia Via Giovanni Pascoli, Milan, Italy. ⁸Present address: Molecular Chirality Research Center, Chiba University, Inage-ku, Chiba, Japan. ✉e-mail: andrew.forbes@wits.ac.za

Supplementary Information: High-purity orbital angular momentum states from a visible metasurface laser

Hend Sroor,¹ Yao-Wei Huang,^{2,3} Bereneice Sephton,¹ Darryl Naidoo,^{1,4} Adam Vallés,^{5,*} Vincent Ginis,^{2,6} Cheng-Wei Qiu,³ Antonio Ambrosio,^{7,8} Federico Capasso,² and Andrew Forbes^{1,†}

¹*School of Physics, University of the Witwatersrand, Private Bag 3, Wits 2050, South Africa*

²*Harvard John A. Paulson School of Engineering and Applied Sciences,*

Harvard University, Cambridge, Massachusetts 02138, USA

³*Department of Electrical and Computer Engineering,*

National University of Singapore, 117583, Singapore

⁴*CSIR National Laser Centre, PO Box 395, Pretoria 0001, South Africa*

⁵*School of Physics, University of the Witwatersrand, Private Bag 3, Wits 2050, South Africa*

⁶*Applied Physics, Vrije Universiteit Brussel, Brussels 1050, Belgium*

⁷*Center for Nanoscale Systems, Harvard University, Cambridge, Massachusetts 02138, USA*

⁸*CNST - Fondazione Istituto Italiano di Tecnologia Via Giovanni Pascoli, 70, 20133 Milano MI, Italy*

Due to the compactness and simplicity associated with the two-mirror cavity design, one may be inclined to try implementing the spin-orbit (SO) coupling laser in such a fashion. It is important to analyse a round trip of such a cavity in order to determine the modes preserved in the system and thus predict the corresponding eigenmodes produced by the laser. A key property of the light determining the output for SO lasers remains in the state of the polarisation as this in turn determines if the OAM produced in each section of the laser cavity, leading to the desired output. Subsequent determination of this relies upon the mode transformations effected by the different elements placed inside the cavity.

One such important factor is the action of the mirrors upon the state of the reflected beam. More specifically, the mirror alters the handedness of both the polarisation and OAM. For instance, right circular polarisation becomes left circular polarisation and OAM of $+\ell$ becomes $-\ell$ upon reflection. This implies that within a complete round trip, the initial states do not return the same. Accordingly, the mode does not self-repeat inside the cavity as shown in Fig. 1 (a). There are some practical alterations, however, that have been implemented to generate a desired eigenstate. One such adjustment was to use a 3 mirror configuration assisted with a pair of both conventional SO coupling elements and quarter-wave plates (QWP) [1]. More recently, however, the authors [2] retained the simplistic two mirror design by incorporating a Faraday rotator with a QWP, allowing control of the polarisation upon each return trip, as illustrated in Fig. 1(b).

These are the works that are most relevant to this study, but the relevance is limited as the discussion was entirely limited to OAM coupling to circular polarisation only, resulting in restricted generation of symmetric OAM states up to $\ell = \pm 10$. Contrarily to these stud-

ies, the presented J-plate laser is designed for arbitrary SO coupling to generate both symmetric and asymmetric OAM modes. Moreover, the coupling to linear polarisation facilitates a very compact design while maintaining self-repeating modes as displayed in Fig. 1(c).

SENSITIVITY OF THE GREEN CAVITY

Figure 2 illustrates the experimental setup for the metasurface laser. The green cavity was oscillating on the fundamental Gaussian mode, however, a slight misaligning the OC mirror (in the empty cavity) might result in higher order modes as shown in Fig. 3. Furthermore, the Gaussian beam size in the green cavity is an important factor when implementing the J-plates inside the cavity. If the beam size is much larger than the size of J-plate's active area, no modulation of light would occur for the lower order mode due to diffraction as shown in Fig. 4.

THE MECHANISM OF THE J-PLATE

The operation of the laser is mainly determined by the operation of the J-plate which acts as a waveplate. Here we provide a discussion of the J-plate's operation in terms of Jones matrices. The Jones matrix for a general waveplate in the linear polarisation basis, is given by

$$U_{\text{WP}} = \begin{bmatrix} e^{i\frac{\beta}{2}} & 0 \\ 0 & e^{-i\frac{\beta}{2}} \end{bmatrix}, \quad (1)$$

where $\beta = \delta_x - \delta_y$ is the phase retardance between the fast and slow axis of the waveplate. The Jones matrix of a rotated version of the general waveplate with fast axis rotated at some angle γ is given by

$$U_{\text{WP}}(\gamma) = R(\gamma) \cdot U_{\text{WP}} \cdot R(-\gamma) = \quad (2)$$

$$\begin{bmatrix} e^{i\frac{\beta}{2}} \cos^2(\gamma) + e^{-i\frac{\beta}{2}} \sin^2(\gamma) & \frac{\sin(2\gamma)}{2} (e^{i\frac{\beta}{2}} - e^{-i\frac{\beta}{2}}) \\ \frac{\sin(2\gamma)}{2} (e^{i\frac{\beta}{2}} - e^{-i\frac{\beta}{2}}) & e^{i\frac{\beta}{2}} \sin^2(\gamma) + e^{-i\frac{\beta}{2}} \cos^2(\gamma) \end{bmatrix},$$

* AV now with Molecular Chirality Research Center, Chiba University, 1-33 Yayoi-cho, Inage-ku, Chiba 263-8522, Japan

† Corresponding author: andrew.forbes@wits.ac.za

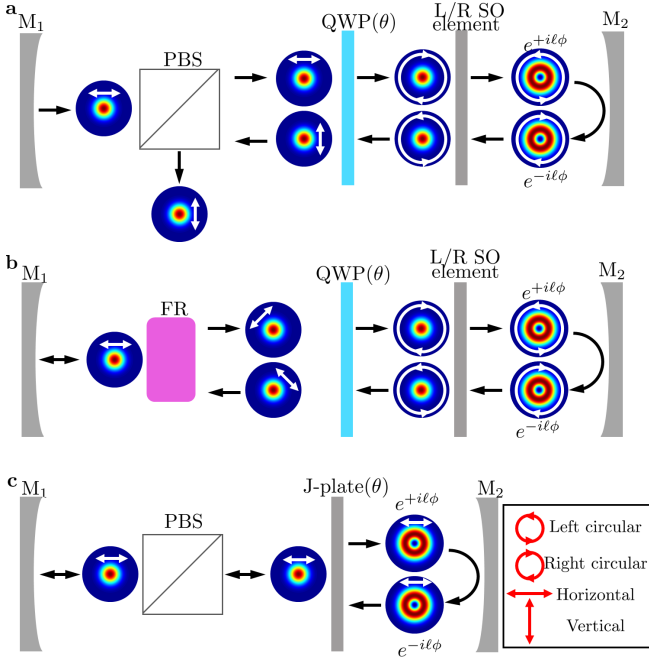


FIG. 1: SO coupling laser configurations. (a) Schematic of a two-mirror laser configuration displays a complete round trip. A horizontally polarised light was selected using a polarising beam splitter (PBS). The polarisation state was converted to a circular polarisation after passing through a rotated quarter-wave plate (QWP). Upon transmission through a spin-orbital (L/R SO) coupling element that is only sensitive to circular polarisation, the incident beam of zero OAM acquire OAM of order ℓ . Upon reflection, the mirror flips both polarisation and OAM state. Acting in reverse, the OAM state collapse and the final state have zero OAM with a polarisation state different to the initial that exist the system through the PBS. (b) shows a complete round trip in the SO laser reported in [2] using a Faraday rotator (FR) to control the polarisation state. (c) A single round trip in the J-plate laser. The inset illustrates the various polarisation states operating in the cavity

where the rotation matrix in the linear polarisation basis is

$$R(\gamma) = \begin{bmatrix} \cos(\gamma) & -\sin(\gamma) \\ \sin(\gamma) & \cos(\gamma) \end{bmatrix}. \quad (3)$$

For example, a rotating half-wave plate with phase retardance $\beta = \pi$ is represented by

$$U_{\text{HWP}}(\gamma) = \begin{bmatrix} \cos(2\gamma) & \sin(2\gamma) \\ \sin(2\gamma) & -\cos(2\gamma) \end{bmatrix}. \quad (4)$$

The J-plate acts as a half-wave plate at the designed wavelength but with a fast axis rotates as a function of the azimuthal angle ϕ and in the linear polarisation basis

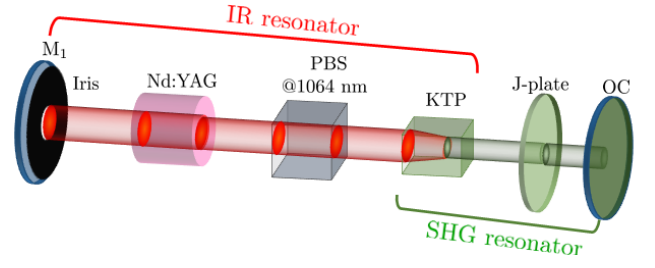


FIG. 2: Experimental metasurface laser setup. The cavity comprised two concave mirrors, M1 and an output coupler (OC) with 99.2% reflectivity. The IR (Nd:YAG) light was converted to second harmonic green using a non-linear KTP crystal. The input (output) faces of the KTP were highly reflective coated for wavelength $\lambda = 532$ nm (1064 nm) and anti-reflective coating for $\lambda = 1064$ nm (532 nm). A polarising beam splitter (PBS) was used to set the intra-cavity polarisation to the horizontal. The fast axis of J-plate was rotatable at an angle θ for the active selection of arbitrary angular momentum beams.

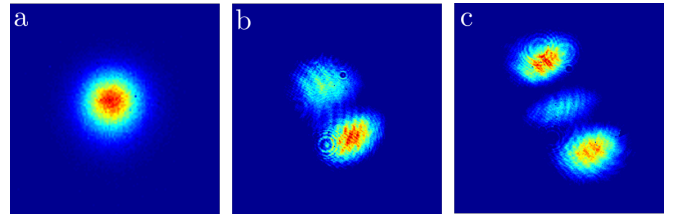


FIG. 3: Modes of the cavity. (a) the fundamental mode of the green laser observed by a CCD camera. (b) and (c) shows the higher order modes when slightly misalign the cavity.

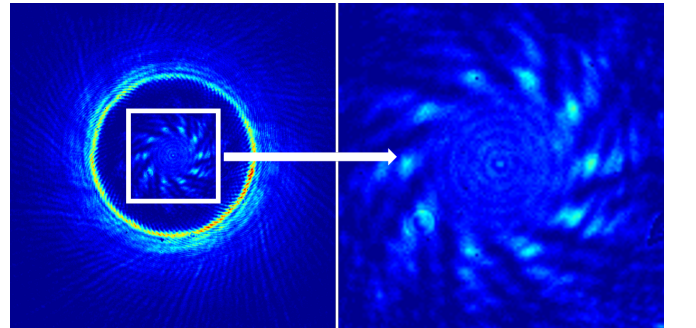


FIG. 4: Effect of beam size on J-plate efficiency. Images show light diffracted from the lower order mode metasurface posts where no extraneous modulation occurs with an incident beam size larger than the active area of the J-plate. The incident beam was 3.2 mm in diameter while the active area of the J-plate was 2 mm in diameter.

is expressed (from Eq. (1)) as

$$U_{JP} = \begin{bmatrix} e^{i\ell_1\phi} & 0 \\ 0 & e^{i\ell_2\phi} \end{bmatrix}, \quad (5)$$

where ℓ_1 and ℓ_2 are two independent OAM values that are acquired by different input polarisation states ($|H\rangle$ and $|V\rangle$), ϕ is the azimuthal angle. The operation of the J-plate converts the input polarisation states to their conjugate polarisation states (still be $|H\rangle$ and $|V\rangle$) [3]. There-

fore, when a Gaussian beam LG₀₀ with linear polarisation states operates on the J-plate, the output states are given by

$$U_{JP} |H\rangle = e^{i\ell_1\phi} |H\rangle = |H, \ell_1\rangle, \quad (6)$$

$$U_{JP} |V\rangle = e^{i\ell_2\phi} |V\rangle = |V, \ell_2\rangle. \quad (7)$$

The Jones matrix for the rotated version of the J-plate in linear polarisation basis [3], similar to Eq. (5), is

$$U_{JP}(\theta) = R(\theta)U_{JP}R(-\theta) = \begin{bmatrix} e^{i\ell_1\phi} \cos^2(\theta) + e^{i\ell_2\phi} \sin^2(\theta) & \frac{\sin(2\theta)}{2}(e^{i\ell_1\phi} - e^{i\ell_2\phi}) \\ \frac{\sin(2\theta)}{2}(e^{i\ell_1\phi} - e^{i\ell_2\phi}) & e^{i\ell_1\phi} \sin^2(\theta) + e^{i\ell_2\phi} \cos^2(\theta) \end{bmatrix}, \quad (8)$$

where θ is the rotation angle of the J-plate. The state input to the J-plate is $|\psi\rangle_{\text{in}} = |H\rangle$. Following the function of J-plate mentioned in Eq. (6) and Eq. (7), the operation of the J-plate with rotation angle θ converts the input state $|\psi\rangle_{\text{in}}$, producing

$$|\psi\rangle_{\text{out}} = U_{JP}(\theta) |\psi\rangle_{\text{in}} = \begin{bmatrix} \cos(\theta)e^{i\ell_1\phi} \\ \sin(\theta)e^{i\ell_2\phi} \end{bmatrix}. \quad (9)$$

The resulting output state can be expressed in the bra-ket notation as

$$|\psi\rangle_{\text{out}} = \cos(\theta) |H, \ell_1\rangle + \sin(\theta) |V, \ell_2\rangle. \quad (10)$$

Note that equation (10) represents a spin-orbital state on the hybrid HOPS.

COHERENT SUPERPOSITION OF LAGUERRE-GAUSSIAN BEAMS

A coherent superposition of higher-order modes is only applicable to mutually coherent beams, i.e. beams that oscillate with the same frequency. This allows for the electric fields of the modes to be simply added together. Here we are particularly interested in the coherently superimposing of two Laguerre-Gaussian LG modes. The electric field of an LG mode at its waist plane ($z = 0$), is described by

$$\begin{aligned} u_{p,\ell}(r, \phi) &= \sqrt{\frac{2p!}{\pi w_0^2(p + |\ell|)!}} \left[\frac{\sqrt{2}r}{w_0} \right]^{|\ell|} L_p^{|\ell|} \left[\frac{2r^2}{w_0^2} \right] \\ &\times \exp \left[\frac{-r^2}{w_0^2} \right] \exp(i\ell\phi), \end{aligned} \quad (11)$$

where p and ℓ are the radial and azimuthal indices, respectively. The parameter w_0 is the radius of the zero-order Gaussian beam at the waist. The term and $L_p^m(\cdot)$ is the generalised Laguerre polynomial and (r, ϕ) are

the spatial (radial and azimuthal) coordinates. The intensity profile formed by such field is $I = u^*u$ (with $*$ representing complex conjugate) and is described by a set of $(p + 1)$ concentric rings. The coherent superposition shown in the main text was modelled as $\alpha u_{0,0} + \beta u_{0,1} + \gamma \exp(i\theta)u_{0,5}$ with the parameters α , β , γ and θ used to adjust for the rotation and efficiency of the J-plate. We find that the $u_{0,0}$ beam requires a slight lateral off-set, probably due to slight misalignment in the cavity.

RADIAL MODES AND OAM PURITY

A pure vortex mode with a fundamental radial index ($p = 0$), is given from Eq. (11) by

$$u_{0,\ell}(r, \phi) = \left[\frac{\sqrt{2}r}{w_0} \right]^{|\ell|} \exp \left[\frac{-r^2}{w_0^2} \right] \exp(i\ell\phi). \quad (12)$$

where the OAM content of the beam is associated with the azimuthal phase $\exp(i\ell\phi)$. Here one can see that the ℓ dependant amplitude term, the first term in the aforementioned equation, is responsible for the distinctive null intensity associated with the vortex. In the absence of this amplitude term, the null intensity in the vortex occurs due to high spatial frequencies induced by the helicity of the phase together with their attenuation due to finite apertures of the optical system.

Traditionally, OAM vortex modes are created by modulating a Gaussian beam with a desired azimuthal phase while ignoring the ℓ dependant amplitude term. Thus the generated beams is expressed as

$$\tilde{u}_\ell(r, \phi) \approx \exp \left[\frac{-r^2}{w_0^2} \right] \exp(i\ell\phi). \quad (13)$$

Implementation of the azimuthal phase approaches to create these beams are revealed to unintentionally generate many undesired radial modes due to the missing

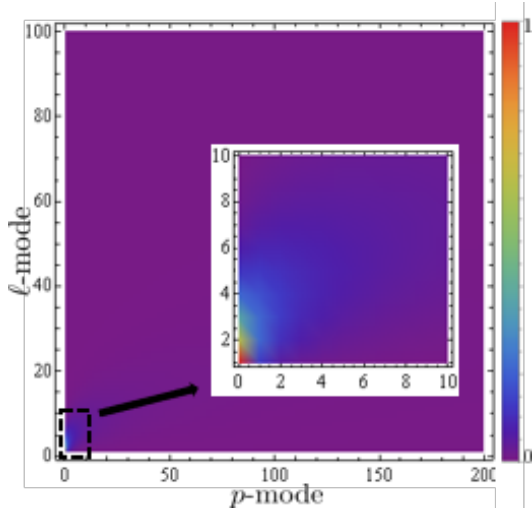


FIG. 5: **Radial modes of vortex beams.** Theoretical density plot, determined from Eq. (15), illustrates the spread of modal weightings $|c_{p\ell}|^2$ of the radial modes for vortex beams generated through external generation approaches that lacks the ℓ -dependant amplitude term in Eq. (12). The inset shows zoomed in images for $\ell = [0, 10]$ and $p = [0, 10]$. (b) shows a comparison for the change in $|c_{p\ell}|^2$ for $\ell = 1$, $\ell = 10$ and $\ell = 100$.

amplitude term (first term in Eq. (12)) [4, 5]. These radial modes appear as rings around the central beam and are usually referred to as Hypergeometric Gaussian modes [6, 7]. They are superpositions of LG modes with the same azimuthal number ℓ , and thus they can be expanded as

$$\exp\left[\frac{-r^2}{w_0^2}\right] \exp(i\ell\phi) = \sum_p c_{p\ell} u_{p\ell}(r, \phi; w_0). \quad (14)$$

Here, $|c_{p\ell}|^2$ is the weightings of the mode of indices p , ℓ and can expressed as

$$c_{p\ell} = \sqrt{\frac{(p+|\ell|)! \Gamma(p + \frac{|\ell|}{2}) \Gamma(\frac{|\ell|}{2} + 1)}{p! \Gamma(\frac{|\ell|}{2}) \Gamma(p+|\ell|+1)}}, \quad (15)$$

where $\Gamma(\cdot)$ is the gamma function. Equation (15) implies that the energy content in the fundamental radial mode ($p = 0$) drops dramatically with increasing azimuthal index ℓ .

If the expansion was changed to a new scale, then the modal power weightings would likewise change, from $c_{p\ell} \rightarrow \hat{c}_{p\ell}$ when $w_0 \rightarrow w_\ell$. With brevity, we illustrate this analytically by maximising the overlap integral between the normalised LG mode and the vortex mode given by

$$c_{p\ell;\alpha} = \mathcal{N}_\ell(\alpha, w_0) \iint u_{p\ell}^*(r, \phi, \alpha w_0) \tilde{u}_\ell(r, \phi; w_0) d^2r, \quad (16)$$

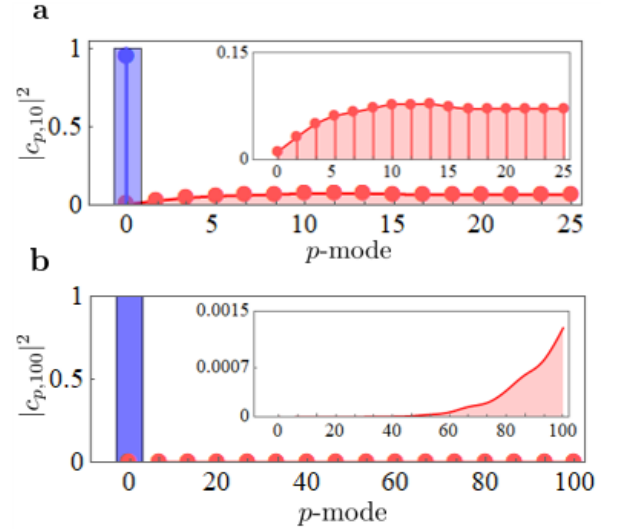


FIG. 6: **Weightings of the radial mode.** Measured modal weightings for (a) $\ell = 10$ and (b) $\ell = 100$, both internal (blue) and external (red) to the laser. Here the experimental data (lollipop bars) are in good agreement with the theoretical predictions (solid line). Measurements were made in the scale w_0 .

where $\mathcal{N}_\ell(\alpha, w_0)$ is the product of normalisation factors for the LG, vortex mode and α scales the size of the LG mode. The overlap has the analytic solution given as

$$c_{\ell;\alpha} = \frac{2^{\frac{|\ell|}{2}} |\ell| \alpha \Gamma\left(\frac{|\ell|}{2}\right)}{(1 + \alpha^2)^{\left(\frac{|\ell|}{2} + 1\right)} \sqrt{\Gamma(|\ell| + 1)}}. \quad (17)$$

Subsequently, the probability $|c_{\ell;\alpha}|^2$ integral is maximised for each ℓ when

$$\alpha = \frac{1}{\sqrt{|\ell| + 1}}, \quad (18)$$

leading to an optimal scale for the decomposition of

$$w_{\text{opt}} = \frac{w_0}{\sqrt{|\ell| + 1}}. \quad (19)$$

Figure 5 shows the spread of the modal modal power across the radial modes as a function of ℓ when measured in the scale w_0 . Here, a vortex mode of $\ell = 1$ has 78% of its energy in the $p = 0$ mode, with the rest spread across higher radial modes. This value drops to $< 1\%$ for $\ell = 10, p = 0$ and to 3×10^{-6} for $\ell = 100, p = 0$. Figure 6 shows the experimental and theoretical prediction of the modal weightings of the radial modes for both $\ell = 10$ and $\ell = 100$ for externally generated beams versus the cavity modes. In Fig. 7, we show the drastic decrease of the $p = 0$ modal weightings on the log scale as a function of the ℓ index.

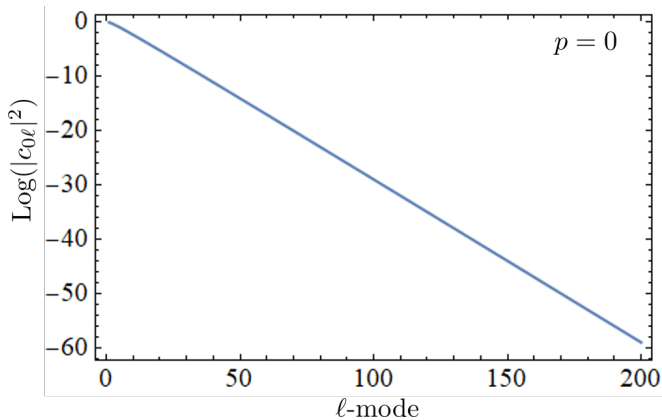


FIG. 7: **Weightings of the $p = 0$ mode as a function of the OAM index.** Theoretical plot, determined from Eq. (15), illustrates the modal weightings $|c_{0\ell}|^2$ on the log scale of the $p = 0$ modes as a function of the OAM index ℓ .

This phenomenon is a natural response to the absence of amplitude modulation. The weightings of the fundamental mode $p = 0$ can be increased by choosing the optimised beam radius w_{opt} in Eq. (14) but keeping the embedded Gaussian the same. Subsequently, this can increase the weightings in the desired $p = 0$ radial mode as illustrated in Fig. 8. For example the $p = 0$ mode can reach up to $|c_{0\ell}|^2 = 0.5$ for $\ell = 10$. The reason for an optimum output beam waist parameter w_{opt} which is smaller than the embedded Gaussian, w_0 , can be understood as follows: for a given beam waist, the root mean square (RMS) intensity radius of an $\text{LG}_{\ell 0}$ mode is larger than the RMS intensity radius of a fundamental Gaussian. Thus if one converts the fundamental Gaussian with a given RMS intensity radius into an $\text{LG}_{\ell 0}$ mode with the same RMS intensity radius, the matching beam radius of the $\text{LG}_{\ell 0}$ mode is necessarily smaller. For higher mode the optimum matching radius becomes even smaller. Thus, the fraction of light converted into higher order radial modes increases with higher ℓ causing reduction in the fractional weightings in the desired $p = 0$ mode, which is still not very convenient.

An interesting outcome of changing the scale of the basis is that the p mode spectrum changes functional shape, as shown in Fig. 9 for the $\ell = 10$ example from the main text. For some scales the trend is a smooth peaked function, while for others it is an oscillatory function, becoming more pronounced as the scale value decreases. This nature has been predicted theoretically [11].

GENERATION OF VECTORIAL VORTEX BEAM WITH SYMMETRIC OAM STATES

In Figure 10(a), we show the experimentally obtained intensity at the output when JP1 is operating inside the laser with $\theta = \pi/4$. The states is represented by

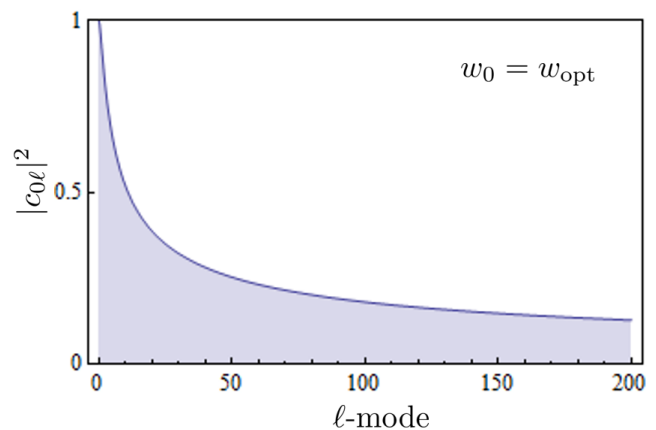


FIG. 8: **Weightings of the $p = 0$ mode after selecting optimised beam size.** Theoretical plot, determined from Eq. (14), illustrates the evolution of the modal weightings $|c_{0\ell}|^2$ of the $p = 0$ radial modes as a function of the OAM index ℓ after selecting the optimised beam size w_{opt} in Eq. (19).

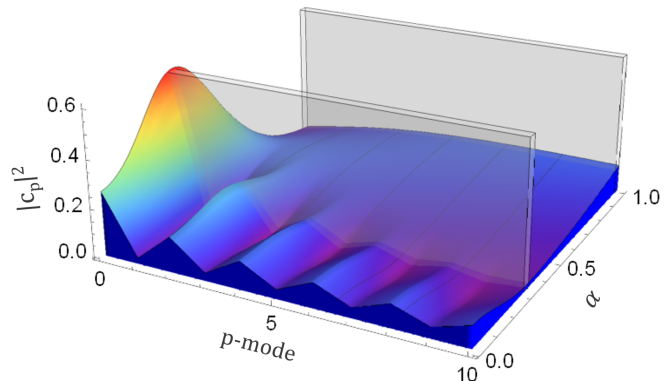


FIG. 9: **The p mode spectrum as a function of basis scale, α , for $\ell = 10$.** The grey planes show the p mode spectrum expected at the original scale w_0 ($\alpha = 1$) and the optimal scale w_{opt} ($\alpha = 1/\sqrt{11}$). The former is a smooth peaked function and the latter an oscillatory function.

$\frac{1}{\sqrt{2}}(|H, -1\rangle + |V, 1\rangle)$. The output beam possessed an annular shaped intensity profile. Upon passing through a polariser, the beam profile changes from the annular shape to a lobed beam depending on the orientation of the polariser. Figure 10 shows a comparison between the experimental results and the theoretical predictions of the spatial profile of the output beam and after succeeding through a polariser with orientations represented by the double sided white arrows. The experimental results have a good agreement with the theoretical predictions, thus presenting a pure vectorial vortex beam located at the equator of the HOPS which is described by $\frac{1}{\sqrt{2}}(|H, -1\rangle + |V, 1\rangle)$. However, these modes can easily be converted to cylindrically vector vortex modes, i.e.

radially and azimuthally polarised vortex modes, by simply passing the beam through a quarter waveplate to flip the polarisation from the linear to circular state.

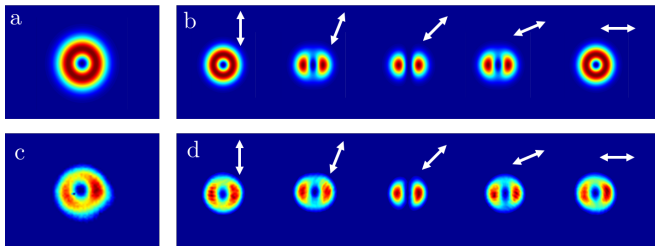


FIG. 10: **Selection of a vectorial vortex beams.**

Pure vectorial vortex beam $\frac{1}{\sqrt{2}}(|H, -1\rangle + |V, 1\rangle)$ is actively selected from the laser while operating on JP1 by setting θ to $\pi/4$. (a) and (c) show the spatial profile of the output beam as theoretically predicted and experimentally captured, respectively. The beam was an annular shaped beam. Upon transmitting through a linear polariser, the beam changes its intensity profile to a lobed beam at polariser orientation angle $\pi/4$. A comparison between the theory (b) and experiment (d) confirms the output beam is a purely vector vortex beam. The inset arrows represent the orientation of the polariser.

POWER MEASUREMENT

We examined the slope efficiency for pure OAM output modes. Figure 11 illustrates the average output energy of each pure OAM mode for the indicated J-plates in comparison to the Gaussian power. One can see that the slope efficiency for $LG_{0,\pm 1}$ modes were approximately similar to the Gaussian which reveal that the JP1 does not lead to high losses inside the cavity. Figure 11 (b) and (c) disclose that higher-order modes generated by JP2 and JP3 introduce higher losses and thus require a higher threshold comparing with JP1 modes.

It is worth mentioning that the slope efficiency was low due to the low transmission of mirror OC which was 0.8%. Therefore most of the cavity power has been locked inside for the examination of the power handling capability of the J-plates which in return showed a potential to be used for the generation of high power HOPS beams, as expected from such elements [8]. Nevertheless, the output coupler could be replaced by another with lower reflectivity in case higher output power is needed.

MODAL DECOMPOSITION

An important technique, essential for analysing the generated beams in terms of established modes, is modal decomposition. This technique is often used for characterising beams, whereby any optical field may be expanded

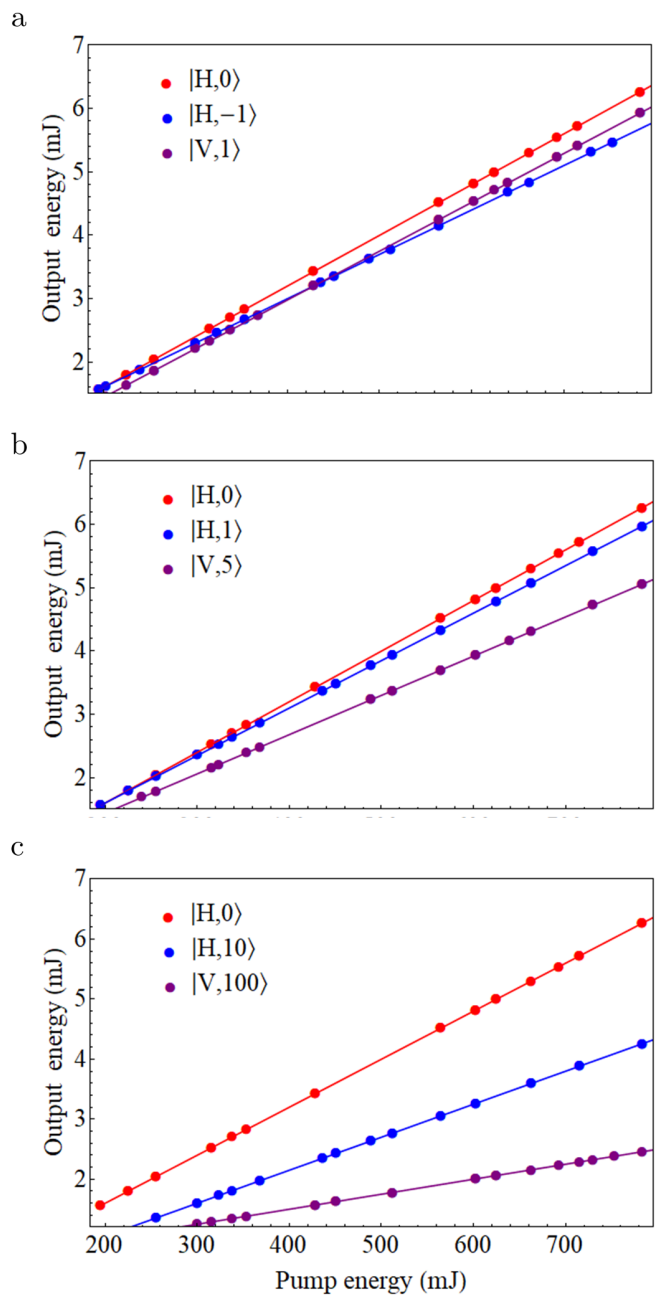


FIG. 11: **Slope efficiency measurements of the OAM cavity.** Average output energy of the secondary cavity for the fundamental Gaussian mode (red data points) of the resonator versus corresponding HOPS beams generated using (a) JP1 ; (b) JP2; and (c) JP3, with the fitting curve of the measurements.

and represented by a linear combination of basis modes as

$$U(\mathbf{r}) = \sum c_{p\ell} \Psi_{p\ell}(\mathbf{r}). \quad (20)$$

Here $\mathbf{r} = (x, y)$ is the spatial coordinate in the transverse plane and $\Psi_{p\ell}(\mathbf{r})$ represents the basis mode. The com-

plex correlation coefficient, $c_{p\ell} = \rho_{p\ell} e^{i\delta\theta_{p\ell}}$ weights the contribution of each of the basis modes where $\rho_{p\ell}$ is the corresponding mode amplitude and $\delta\theta_{p\ell}$ the intermodal phase difference between the ℓ mode and a selected reference mode. The determination of the coefficients $c_{p\ell}$ which are normalised according to

$$\sum_{p,\ell} |c_{p\ell}|^2 = 1, \quad (21)$$

may be determined by executing an inner product between the input field and a desired basis mode, which is given as

$$c_{p\ell} = \langle U | \Psi_{p\ell} \rangle = \iint_{\mathcal{R}} U(r) \Psi_{p\ell}^*(r) d^2r, \quad (22)$$

where the asterisk represents the complex conjugate. The determination of the modal weightings allows decomposing the optical field into its basis modes. Optically, these modal weightings are determined by measuring the resultant field $u(x, y) = U(x, y) \Psi_{p\ell}^*(x, y)$ at the Fourier plane where the corresponding transformation is expressed as

$$\tilde{U}(k_x, k_y) = \mathcal{F}\{u(x, y)\} = \iint U(x, y) \Psi_{p\ell}^*(x, y) e^{-i(k_x x + k_y y)} dx dy. \quad (23)$$

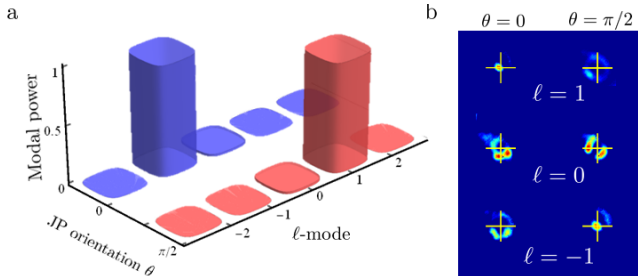


FIG. 12: **JP1 modes measurements.** A modal decomposition measurements are executed on the output of JP1 laser operating under $\theta = 0$ and $\pi/2$ illustrating (a) a pure $LG_{0,-1}$ and $LG_{0,1}$ mode, respectively, with (b) the raw data where on-axis intensity (as indicated by the cross-hairs) means existence of the mode while no intensity indicates the mode's absence.

The modal weightings $c_{p\ell}$ in Eq. (22) are optically determined by measuring the on-axis intensity of the field $\tilde{U}(k_x, k_y)$ by setting the propagating vectors $k_x = k_y = 0$, thus Eq. (23) is expressed as:

$$I(0, 0) = |\tilde{U}(0, 0)|^2 = \left| \iint U(x, y) \Psi_{p\ell}^*(x, y) dx dy \right|^2.$$

Experimentally, this characterisation technique may be implemented with the use of a spatial light modulator

(SLM). In this scenario, unknown field $U(x, y)$ is directed toward the SLM which is digitally encoded with a matching filter $\Psi_{p\ell}^*(x, y)$ with unique carrier frequency to separate the first order diffraction from the undesired order of diffraction. The resultant field was transformed in the Fourier plane using a Fourier lens which was positioned at the focal length from the plane of the SLM. The on-axis intensities at the Fourier plane after the lens were recorded using a CCD camera, where an on-axis signal dictated a correlation between the generated mode and match filter, while an on-axis null indicated a mismatch.

This technique was executed at on the output of the JP1 cavity. The basis set for the decomposition was chosen to be the Laguerre Gaussian ($LG_{p,\ell}$) set and the transmission functions were varied from $\ell = -2$ through to 2 as as illustrated in Fig. 12(a), we obtained an on-axis intensity signal for a Laguerre Gaussian mode with $\ell = -1$ and $+1$ for JP1 orientations $\theta = 0$ and $\pi/2$, respectively, with zero for all other modes. Figure 12(b) shows the corresponding intensity of the measurement channels at the Fourier plane.

The modal decomposition was performed in real-time on the output of JP2 cavity to determine the modal fractional, i.e. the relative weightings between the $\ell = 1$ and $\ell = 5$ modes. The output of the cavity passed through a polarising beam splitter (PBS) where the horizontal and vertical components were separated. Each polarisation component was then directed toward two halves of a single SLM which were encoded with appropriate matching filters. This resulted two outputs on the CCD camera. The on-axis intensities, $I_H(0, 0)$ and $I_V(0, 0)$, were then subtracted from the system background noise ϵ

$$\bar{I}_i(0, 0) = I_i(0, 0) - \epsilon, \quad (24)$$

where $i = \{H, V\}$. The modal fractional of each mode was evaluated by normalising the on-axis intensity to the total on-axis intensities

$$\text{Modal fraction} = \frac{\bar{I}_i(0, 0)}{\sum_i \bar{I}_i(0, 0)}. \quad (25)$$

The results are illustrated as a function of the J-plate orientation (θ) in Fig. 2c.

CONVERSION EFFICIENCY OF THE J-PLATES

The basis scale determines the maximum power content in the $p = 0$ mode for a given OAM content, as given by the earlier equations. The product of the two gives the maximum power content in the desired ℓ and $p = 0$ mode. For example, an externally generated $\ell = 100$ mode has a measured $\ell = 100$ OAM content of 71%, and with an optimal decomposition the $p = 0$ component is then $71\% \times 18\% = 13\%$.

TABLE I: Conversion efficiencies into the $p = 0$ mode of the externally generated modes using different J-plates and an optimal basis.

Mode	Maximum $p = 0$ purity	Total OAM content	OAM $p = 0$ purity
JP1: $ H, -1\rangle$	93%	88%	82%
JP1: $ V, 1\rangle$	93%	88%	82%
JP2: $ H, 1\rangle$	93%	95%	89%
JP2: $ V, 5\rangle$	69%	83%	57%
JP3: $ H, 10\rangle$	53%	72%	38%
JP3: $ V, 100\rangle$	18%	71%	13%

EMISSION SPECTRUM OF THE J-PLATE LASER

We examined the emission spectrum of the output beam from the green laser. We used a spectrometer produced by Ocean Optics (USB4000). The emission spectrum of the laser beam shows a single peak at wavelength 532 nm as shown in Fig. 13.

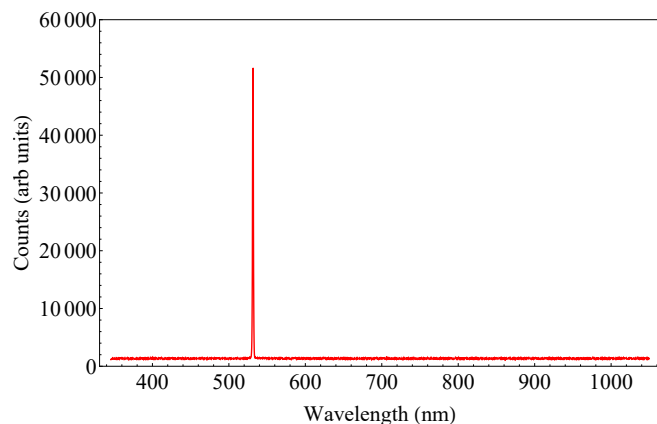


FIG. 13: **Emission spectrum measurement.** Emission spectra of the metasurface laser shows a single intensity peak at $\lambda = 532$ nm.

CREATING ARBITRARY HOPS LASER BEAMS

We have outlined the concept for a new class of laser that utilises metasurface J-plates to realise symmetric and asymmetric OAM beams on the HOPS. We have shown the lasing mode can be tuned from one pole of the HOPS to the other by controlling the relative amplitude between the OAM states, following the blue trajectory on the HOPS shown in Fig. 14.

We point out that this concept extends to map any arbitrary mode on the HOPS. This requires controlling the relative phase between the states to allow mapping the states along the red trajectory in Fig. 12, which can be achieved by controlling the ellipticity of the polarisation

inside the green laser.

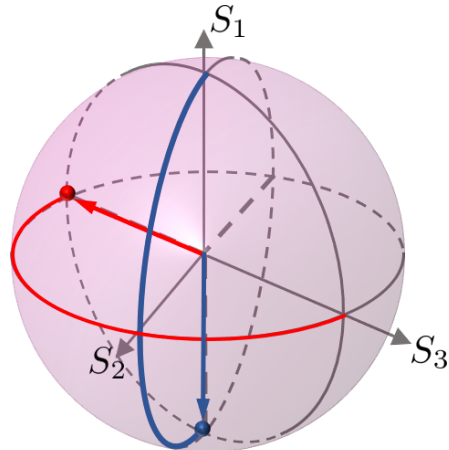


FIG. 14: **Mapping arbitrary HOPS beams.** Any arbitrary HOPS beam can be generated from our metasurface laser. While controlling the orientation of the J-plate maps any the states from the north to the south pole of the HOPS (blue trajectory), manipulating the polarisation ellipticity of the pump beam maps any states at the equator (red trajectory).

For example if the IR pump could be an external laser, implementation of a quarter wave plate would allow tuning the ellipticity of the pump polarisation and thus controlling the relative phases of the output of the other laser. This only occurs by appropriately selecting the non-linear KTP crystal as shown in Refs. [9, 10]. Dynamically tuning the pump's polarisation would result in a controllable output mode from a laser requiring no intra-cavity elements other than the metasurface itself, which would remain static. This would allow to transverse the entire HOPS in a controllable manner.

PURITY MECHANISM INSIDE THE CAVITY

There are several mechanisms that contribute to the purity of the observed modes from the laser. First, the green cavity can be modelled as an optical parametric oscillator (OPO) cavity of hemispherical type so that the resonant modes are given by a frequency spectrum of

$$\nu_{q\ell} = \left(q + (2p + |\ell| + 1) \cos^{-1} \frac{\sqrt{g_1 g_2}}{\pi} \right) \frac{c}{2L}, \quad (26)$$

where $g_1 = 1 - L/R_1$ and $g_2 = 1 - L/R_2$ are the resonator parameters. In our green cavity: $L \approx 197$ mm and was adjusted by a few mm in each run, $R_1 = \infty$ and $R_2 = 200$ mm so that

$$\nu_{q\ell}/\nu_0 \approx q + \frac{1}{2}N, \quad (27)$$

with $\nu_0 = c/2L$ and $N = 2p + |\ell| + 1$ is the transverse mode number. In terms of bandwidth this is simply

$$\Delta\nu_{qpl}/\nu_0 = \Delta q + \frac{1}{2}\Delta N \approx 10^2. \quad (28)$$

Such a cavity is frequency degenerate in transverse mode number (N), but while the empty cavity cannot distinguish between a change in ℓ and a change in p if N doesn't change, the J-plate cavity can - it has an ℓ selective intra-cavity element. Next, taking into account that the non-linear crystal is pumped by a Gaussian mode, and factoring in mode coupling inside the OPO cavity, then the allowed spectrum of radial modes about some ℓ is substantially reduced, with a coupling efficiency given by [12]

$$\eta_p = \frac{(2p)!}{(2^p p!)^2}, \quad (29)$$

which is plotted in Fig. 15. The parametric interaction is not very selective as far as transverse modes are concerned, but will oscillate on modes with the lowest threshold. Since the green cavity allows modes about $\Delta p \approx 10$ we could tune for resonance for each ℓ successfully. Our cavity was length adjusted with and without the J-plate, which we found helped to suppress radial modes, which we understand as a resonance condition of the cavity.

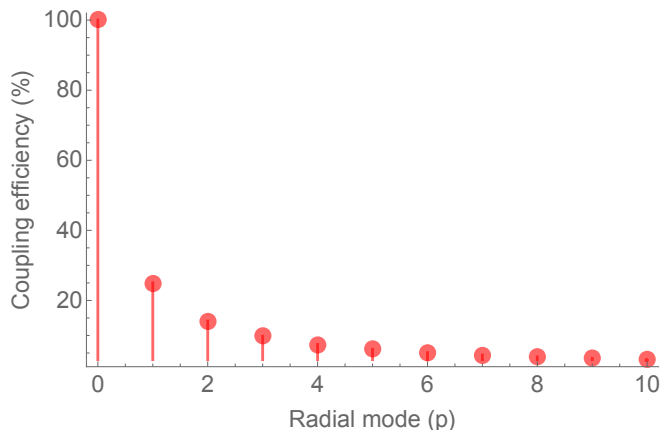


FIG. 15: Allowed modes in the cavity considering only the pump and SHG beams in the green cavity.

Next, our metasurface laser is designed to morph the beam from one shape at the crystal end to another at the OC end. A Fox-Li simulation [13] of the cavity reveals that indeed the resonant mode of the cavity is the desired mode in amplitude and phase, shown in Fig. 16 (a) and (b). Here the $\ell = 10$ case (as an example) is shown to converge, starting from noise, finally revealing that the lowest loss mode in the cavity has the expected phase and amplitude - a high-purity OAM mode with no radial modes. The simulation also reveals that the lowest

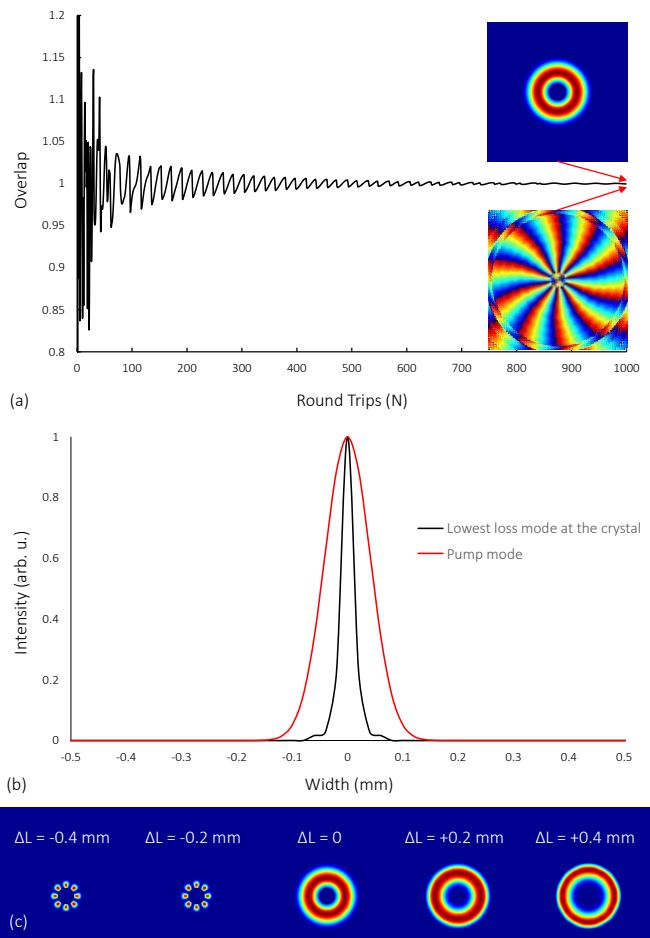


FIG. 16: (a) A Fox-Li simulation of the green cavity mode for the $\ell = 10$ case. The simulation starts from noise and then converges to the mode experimentally observed from the laser, both in amplitude and phase (shown as insets). (b) The mode at the crystal overlaps well with the IR Gaussian pump for gain assisted filtering. (c) Shows the lowest loss transverse mode at the output as a function of cavity length: the cavity length too must be carefully adjusted or the modal purity is adversely affected.

loss mode changes with cavity length, as expected from the aforementioned theory. This is shown in the bottom panel of Fig. 16 (c) for small changes in the cavity length, ΔL .

The mode at the KTP crystal however is not Gaussian but rather is Gaussian-like - a beam with a Gaussian envelop as shown in Fig. 16 (b). The deviation from Gaussian is enough to ensure that during propagation from the crystal to the J-plate the mode acquires the necessary amplitude term to negate the creation of radial modes (recall the radial modes appear as a consequence of the missing amplitude term). The pump laser was operated on the fundamental Gaussian mode ($p = 0$) and overlapped the Gaussian-enveloped modes of the green

for all ℓ ; as a result, and as shown by the simulation of the cavity, the high-purity mode of the cavity was also the lowest loss mode of the cavity by virtue of gain-assisted filtering [14, 15].

All OAM modes in the cavity must have identical wavefront curvature at the OC, and hence have the same Rayleigh length z_r . Our simulations of the cavity confirm this - the embedded Gaussian size of the OAM mode (the scale parameter of the mode, w_0) is the same for all modes at the OC. Due to the reciprocity of light, the OC

works as a conjugate mirror for all ℓ , returning the modes to the metasurface exactly as they left it. This inverse step unwraps the helicity but maintains the radial mode structure.

Together then the cavity suppresses radial modes by a combination of diffraction-induced filtering, resonance-induced filtering and gain-assisted filtering. The result is that higher-order radial modes are not resonant, experience additional loss, and for these reasons the resonant mode is predominately the $p = 0$ term.

-
- [1] Naidoo, D., *et al.* Controlled generation of higher-order Poincaré sphere beams from a laser. *Nat. Photonics* **10**, 327-332 (2016).
- [2] Maguid, E., *et al.* Topologically Controlled Intracavity Laser Modes Based on Pancharatnam-Berry Phase. *ACS Photonics* **5**, 1817-1821 (2018).
- [3] Devlin, R.C., Ambrosio, A., Rubin, N.A., Mueller, J.B. & Capasso, F. Arbitrary spin-to-orbital angular momentum conversion of light. *Science* **358**, 896-901 (2017).
- [4] Rafayelyan, M. & Brasselet, E. Laguerre-Gaussian modal q-plates. *Opt. Lett.* **42**, 1966-1969 (2017).
- [5] Rafayelyan, M., Gertus, T. & Brasselet, E. Laguerre-Gaussian quasi-modal q-plates from nanostructured glasses. *Appl. Phys. Lett.* **110**, 261108 (2017).
- [6] Karimi, E., Zito, G., Piccirillo, B., Marrucci, L. & Santamato, E. Hypergeometric-gaussian modes. *Opt. Lett.* **32**, 3053-3055 (2007).
- [7] Sephton, B., Dudley, A. & Forbes, A. Revealing the radial modes in vortex beams. *Appl. Opt.* **55**, 7830-7835 (2016).
- [8] Yao, J., *et al.* Investigation of damage threshold to TiO₂ coatings at different laser wavelength and pulse duration. *Thin Solid Films* **516**, 1237-1241 (2008).
- [9] Zambon, N.C., *et al.* Optically controlling the emission chirality of microlasers. *Nature Photon.* **13**, 283 (2019).
- [10] Taira, T., Sasaki, T. & Kobayashi, T. Polarization control of Q-switch solid-state lasers with intracavity SHG crystals. *Electron. Commun. Jpn 2* **75**, 1-12 (1992).
- [11] Vallone, G. Role of beam waist in Laguerre-Gauss expansion of vortex beams. *Opt. Lett.* **42**, 1097-1100 (2017).
- [12] Schwob, C., Cohadon, P.F., Fabre, C., Marte, M.A.M., Ritsch, H., Gatti, A. & Lugiato, L. Transverse effects and mode couplings in OPOS. *Appl. Phys. B* **66**, 685-699 (1998).
- [13] Fox, A.G. & Li, T. Resonant modes in a maser interferometer. *Bell Labs Tech. J.* **40**, 453-488 (1961).
- [14] Lukishova, S.G., *et al.* High-power laser beam shaping using apodized apertures. *Laser and Part. Beams* **8**, 349-360 (1990).
- [15] Southwell, W. H. Using apodization functions to reduce sidelobes in rugate filters. *Appl. Opt.* **28**, 5091-5094 (1989).